Publication IV

Arttu Polojärvi and Jukka Tuhkuri. On modeling cohesive ridge keel punch through tests with a combined finite-discrete element method. ***Cold Regions Science and Technology*****, 85, 191-205, 2013.**

Cold Regions Science and Technology 85 (2013) 191–205

Contents lists available at SciVerse ScienceDirect

Cold Regions Science and Technology

journal homepage: www.elsevier.com/locate/coldregions

On modeling cohesive ridge keel punch through tests with a combined finite-discrete element method

Arttu Polojärvi *, Jukka Tuhkuri

Aalto University, School of Engineering, Department of Applied Mechanics, P.O. Box 14300, FI-00076 Aalto, Finland

ARTICLE INFO

Article history:
Received 3 July 2012
Accepted 17 September 2012

Keywords:
Ice rubble
Punch through tests
Freeze bonds
Numerical modeling
Combined finite-discrete element method
Cohesive elements

ABSTRACT

This paper introduces a technique for modeling partly consolidated ice rubble using a two-dimensional combined finite-discrete element method and an application of the technique on ice rubble punch through experiments. In the technique, each ice block within the rubble, the contact forces between the blocks, the block deformation, and the rubble freeze bonds are modelled. Simulations with various freeze bond strengths and block to block friction coefficients were performed. As a main simulation result, the close relationship between rubble deformation patterns and load records is demonstrated in detail. It is shown that the buoyant load component due to the rubble becoming detached from the surrounding rubble field and displaced during an experiment is of crucial importance when interpreting punch through experiment results. The consequences of simulation results on ice rubble material modeling are discussed.

1. Introduction

Ice ridges are common features in northern seas. Two of the most important parts of ice ridges are the consolidated layer, which is comprised of frozen water and ice blocks, and the keel, which consists of ice rubble. The rubble can be a collection of loose blocks, but it is often partly consolidated, that is, it consists of ice blocks bonded together by freeze bonds, which resist the relative movement of the blocks. The freeze bonds are formed due to freezing or sintering (Ettema and Schaefer, 1986; Kuroiwa, 1961).

Punch through experiments are commonly used to test the properties of ice rubble. In a punch through experiment, a flat indentor platen penetrates the rubble mass while the force applied by the rubble on the indentor is measured. The indentor force-displacement records, together with the dimensions of the experimental set up, are then used to derive some of the material properties of the rubble.

The first punch through experiments were performed by Leppäranta and Hakala (1989, 1992) using a loading platform and concrete blocks. Since then, the experimental equipment has been improved and the method has been used in full scale as reported by, for example, Bruneau et al. (1998), Heinonen and Määttänen (2000, 2001a,b), Croasdale et al. (2001) and Heinonen (2004). For more detailed analysis of the behavior and failure mechanism of rubble in punch through tests, experiments in laboratory scale have been performed by, for example, Leppäranta and Hakala (1992), Bruneau et al. (1998), Azarnejad et al. (1999), Azarnejad and Brown (2001), Jensen et al. (2001), Lemee and Brown (2002), Serré (2011) and Polojärvi and Tuhkuri (2012). Liferov and Bonnemaire (2005) have reviewed the experimental work and modeling.

The modeling of punch through experiments using continuum models has been performed by a number of authors. These models have been successful in replicating full scale (Heinonen, 2004) and laboratory (Liferov et al., 2003; Serré, 2011) experiments, but have the disadvantage that the details about the rubble behavior have been smoothed out from the modeling results due to the continuum description of the rubble. One such detail has to do with the relation of rubble mass transfer to indentor load records as addressed in Polojärvi et al. (2012) in the case of non-cohesive rubble.

Hence, even if the ice rubble usually consists of multitude of ice blocks, it remains unclear whether or not there are enough blocks to describe the rubble as a continuum, and thus, if the continuum models can always reliably be used for rubble. This motivates the discontinuous approach, in which rubble is modelled block by block, used here. We believe, that this approach helps in gaining more understanding on the phenomena behind ice rubble behavior. This understanding can then be used not only in the estimation of ice loads or in the planning of future experiments, but also in making further improvements to the more commonly used continuum models.

This paper presents a technique for modeling partly consolidated ice rubble using a discontinuous approach, and modeling of punch through experiments using the technique. The traditional way of modeling discontinuum is the discrete element method (DEM), which dates back to Cundall and Strack (1979). In DEM, the individual particles are usually assumed rigid, and their deformation is taken into account in the inter-particle contact models. In the present study, however, the blocks within the keel are deformable and the combined finite-discrete element method (FEM-DEM) is used (Munjiza, 2004; Munjiza and Andrews,

* Corresponding author. Tel.: +358 9 470 23438.
E-mail address: arttu.polojarvi@aalto.fi (A. Polojärvi).

0165-232X/$ – see front matter © 2012 Elsevier B.V. All rights reserved.
http://dx.doi.org/10.1016/j.coldregions.2012.09.013

2000; Munjiza et al., 1995). Cohesive elements were used to model freeze bonds binding the blocks within the rubble together (Block et al., 2007; Camacho and Ortiz, 1996; Morris et al., 2006; Ortiz and Pandolfi, 1999; Sam et al., 2005).

The numerical modeling of ice rubble related problems using DEM and FEM-DEM has previously been used in studies on ice ridging (Hopkins, 1992, 1998; Hopkins et al., 1999), ice pile-up against structures (Haase et al., 2010; Paavilainen and Tuhkuri, 2012; Paavilainen et al., 2006, 2009, 2011) and punch through experiments on unconsolidated rubble (Polojärvi and Tuhkuri, 2009; Polojärvi et al., 2012; Tuhkuri and Polojärvi, 2005). Different types of cohesive models have been previously used in modeling sea ice fracture by, for example, Mulmule and Dempsey (1997a,b, 1999), Bazant (2002), Schreyer et al. (2006), Gürtner (2009) and Dempsey et al. (2010).

This paper first discusses the mechanics of the simulations. The emphasis of this part of the paper is on the modeling of the freeze bonds between the individual rubble blocks. This is followed by a description on the application of the model on the study of ridge keel punch through experiments. After this, we present the results and analyze them in detail, and provide a discussion on them. Finally, the paper concludes with some remarks on and suggestions for future work.

2. Description of the simulations

The virtual punch through experiments were performed using the combined finite-discrete element method (FEM-DEM). In this method, the discrete elements representing the ridge keel blocks are meshed into finite elements. The finite elements are used to compute the block deformation and the contact forces between colliding blocks. In addition to contact forces, the deformation and the motion of the blocks is caused by inertial forces and cohesive forces, and by buoyant force, which is caused by water.

The simulations were explicit and central difference method was used to advance between the time steps. On each time step of a simulation, the following seven tasks are performed: (1) Determination of internal forces according to the displacement field for continuous material, (2) a neighbor search, (3) derivation of contact forces, (4) stress state check at freeze bonds, (5) calculation of the cohesive forces in the material points under failure process, (6) adding external forces, and (7) updating of node positions using Newton's laws for the next time step.

2.1. Contact forces

The contact forces were derived using a penalty function and the potential contact force method (Munjiza, 2004; Munjiza and Andrews, 2000; Munjiza et al., 1995). In the potential contact force method, a potential φ with continuous first partial derivatives with respect to spatial coordinates is defined for every point P of each finite element area Γ. Further, $\varphi = \varphi(P)$ should vanish on finite element edge S for a smooth collision response. Hence,

$$\varphi(P) > 0, \quad P \in \Gamma \quad \wedge \quad \varphi(P) = 0, \quad P \in S. \tag{1}$$

When triangular finite elements are used, an obvious choice for $\varphi(P)$ is the area coordinates.

The contact force, $\mathrm{d}\mathbf{f}_\varphi$, applied to an infinitesimal area element, $\mathrm{d}\Gamma_o$, penetrating into φ is determined from the gradient of φ as (Fig. 1a)

$$\frac{\mathrm{d}\mathbf{f}_\varphi(P)}{\mathrm{d}\Gamma_o} = -s\nabla\varphi(P), \tag{2}$$

where s is a positive constant penalty term. The negative sign is due to the repulsive nature of the contact force. The contact force, $\mathbf{f}_\varphi$, due to $\varphi(P)$ is determined by integration over the overlap area, Γ_o,of two colliding elements. The integral is reduced to a computationally more efficient integral over the boundary of area $\mathrm{d}\Gamma_o$ using a generalized version of Gauss's theorem:

$$\mathbf{f}_\varphi = -s\int_{\Gamma_o} \nabla\varphi(P)\mathrm{d}\Omega = -s\int_{S_o} \varphi(P)\mathbf{n}\ \mathrm{d}\Gamma, \tag{3}$$

where $\mathbf{n}$ is the unit outer normal of S_o (Fig. 1b). The previous equation shows that the distributed load acting upon overlapping volume elements due to φ is reduced to a force acting upon a single point on S_o.

Dissipation due to sliding friction is modelled using dynamic Coulomb friction. The frictional force, $\mathbf{f}_\mu$, is solved using the following equation:

$$\mathbf{f}_\mu = -\mu|\mathbf{f}_c|\frac{\mathbf{v}_r - \mathbf{v}_r\cdot\mathbf{n}}{|\mathbf{v}_r - \mathbf{v}_r\cdot\mathbf{n}|}, \tag{4}$$

where μ is the friction coefficient and $\mathbf{v}_r - \mathbf{v}_r\cdot\mathbf{n}$ is the tangential component of the relative velocity of contacting blocks at the point of contact.

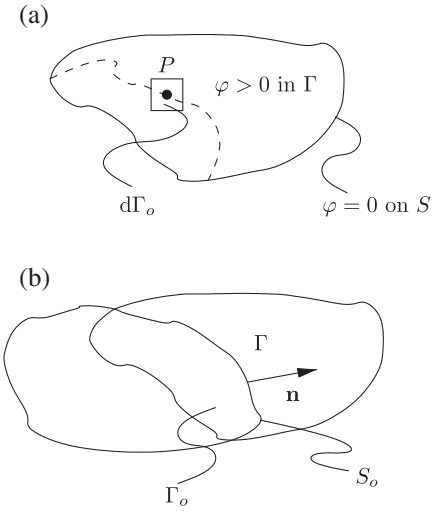

Fig. 1. (a) An infinitesimal area element $\mathrm{d}\Gamma$ at point P penetrating a finite element with area Γ and (b) the overlap area $\mathrm{d}\Gamma_o$ of two elements.

2.2. Block deformation

Though large displacements of individual ice blocks are allowed in the simulations, the deformation of material elements within the continuous ice blocks was assumed to be small. The material behavior of the continuous ice blocks is thus assumed to be linear elastic. This assumption is justified because, rather than being dominated by the deformation of the individual ice blocks, the deformation of the ice rubble is dominated by inter-particle sliding and the movement of the blocks within the rubble (Heinonen, 2004; Sayed et al., 1992).

Furthermore, the material behavior of the blocks is assumed to be isotropic and plane strain state is assumed. The material damping of the blocks on the elastic regime is viscous. Internal forces due to the deformation of the blocks are solved using constant strain triangle elements with an explicit solution procedure implemented as presented in detail by Munjiza (2004).

2.3. Freeze bonds

The freeze bonds were modelled using initially rigid cohesive elements (Block et al., 2007; Camacho and Ortiz, 1996; Morris et al., 2006; Ortiz and Pandolfi, 1999; Sam et al., 2005). In this approach, the finite element mesh is initially continuous. Once the stress state in some point of the mesh (here in point belonging to a freeze bond) fulfills a predefined failure criterion, an energy dissipating cohesive crack growth process at that point begins. The approach was used here, as Fig. 2 illustrates: The simulated keel was meshed in its initial configuration with the mesh being continuous over the contacting surfaces of the blocks.

As Fig. 2 further shows, the edges of the finite elements connecting the blocks were defined as freeze bonds. The failure within the rubble was limited to only on the freeze bonds in order to study their effect on rubble failure. On each time step of a simulation, the stress state at each freeze bond point (a finite element mesh node belonging to a freeze bond) was monitored and compared to a failure criterion, as presented below. Once the failure criterion at a freeze bond point was reached, the point underwent a cohesive crack growth process, which is described below.

2.3.1. Failure criterion

The failure criterion for the freeze bonds is as follows:

$$t_e \geq \sigma_{cr}, \tag{5}$$

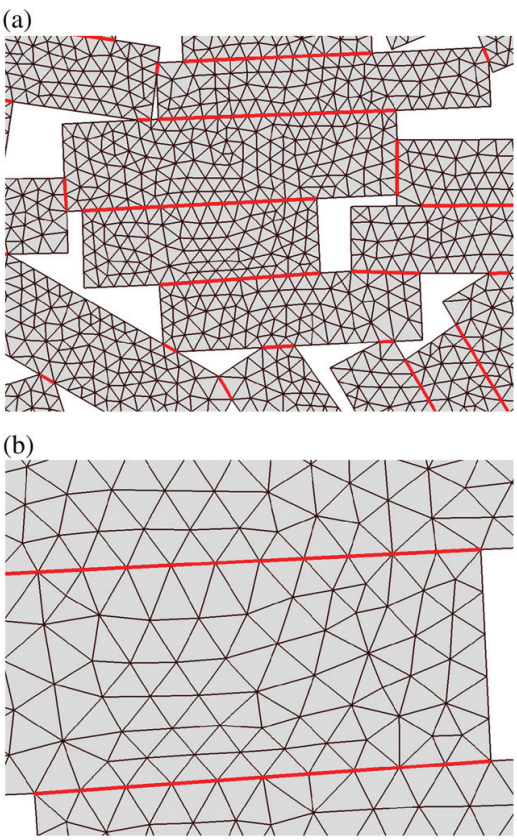

Fig. 2. Two snapshots from a simulation: (a) Ice blocks bonded together by freeze bonds (red) and (b) a close-up of two freeze bonds.

where t_e is the effective traction at a bond point defined as

$$t_e = \begin{cases} \sqrt{\beta^{-2} t_t^2 + t_n^2} & \text{if } t_n \geq 0 \\ \beta^{-1}(|t_t| - \mu |t_n|) & \text{if } t_n < 0. \end{cases} \tag{6}$$

In the definition for t_e, t_t and t_n are the tangential and normal components of the traction vector $\mathbf{t}$ at a bond point, respectively, and μ is the friction coefficient. Furthermore, β is the shear stress factor, defined as $\beta = \tau_{cr}/\sigma_{cr}$, where τ_{cr} and σ_{cr} are the shear and tensile strengths of the bond, respectively. The failure criterion is for a mixed mode fracture, as the definition for t_e shows. In addition, for shear failure under compression, the criterion takes into account the contact friction, as discussed in the next section.

The traction vector, $\mathbf{t}$, is solved here similarly to Block et al. (2007) using the area weighted average of the elastic stresses of the elements connected to the bond point:

$$\mathbf{t} = \sum_{i=1}^{n} \left(\frac{A_i}{A} \right) \sigma_i \mathbf{n}. \tag{7}$$

In the previous equation, A_i and σ_i are the area and elastic stress tensor, respectively, of the element i, A is the total area of n elements connected to the point, and n is the bond surface normal.

2.3.2. Cohesive crack growth

When cohesive crack growth is initiated at a freeze bond point, the finite element mesh node is splitted into two nodes with initially equal nodal coordinates, $\mathbf{x}^+$ and $\mathbf{x}^-$, as shown in Fig. 3a and b. The mass, m, of the node before splitting is divided by the new nodes according to the elements connected to the node; hence $m^+ + m^- = m$. It should be noted, that here lumped masses are assumed.

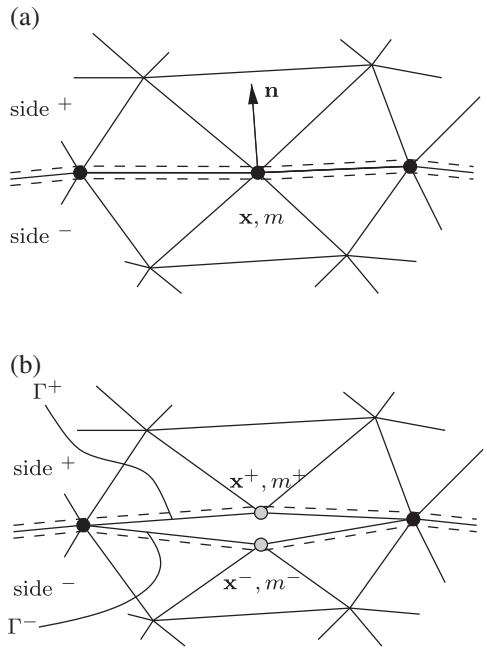

Fig. 3. An illustration of the bond splitting process: (a) An intact node belonging to the bond surface (between the dashed lines) with a normal $\mathbf{n}$, nodal coordinate $\mathbf{x}$, and mass m is split into (b) two nodes with masses m^+ and m^- and the nodal coordinates $\mathbf{x}^+$ and $\mathbf{x}^-$. Similarly, new crack surfaces Γ^+ and Γ^- are generated.

During the cohesive crack growth, a nodal cohesive force, $\mathbf{f}_c = \mathbf{f}_c^+ = -\mathbf{f}_c^-$, resisting the cohesive crack opening is applied to the newly generated nodes similarly to the work of Block et al. (2007). The initial value, $|\mathbf{f}_c^0|$, is derived as follows. The elements connected to node $^{+(-)}$ are used to compute the internal force vector $\mathbf{f}^{+(-)}$ for the stress state $t_e = \sigma_{cr}$ (Eq. (5)). Then, $\mathbf{f}^{+(-)}$ are used to solve the initial value $|\mathbf{f}_c^0|$ from (Block et al., 2007; Papoulia and Vavasis, 2003; Sam et al., 2005):

$$\left|\mathbf{f}_c^0\right| = \left| -\frac{m^-}{m}\mathbf{f}^+ + \frac{m^+}{m}\mathbf{f}^- \right|. \tag{8}$$

As the distance between the nodes $^-$ and $^+$ increases during the crack growth, the value of cohesive force $|\mathbf{f}_c|$ decreases following the linear softening law illustrated in Fig. 4. As the figure shows, $|\mathbf{f}_c|$ is a function of effective crack opening displacement (Camacho and Ortiz, 1996; Ortiz and Pandolfi, 1999; Sam et al., 2005)

$$\delta_e = \sqrt{\beta^2\delta_t^2 + \langle\delta_n\rangle^2}, \tag{9}$$

where δ_t and δ_n are the components of the cohesive crack opening displacement, $\boldsymbol{\delta} = \mathbf{x}^+ - \mathbf{x}^-$, to the tangential and normal directions of the freeze bond, respectively. The operator $\langle\rangle$ in the definition is the Macaulay brackets; hence $\langle\delta_n\rangle = 0$ if $\delta_n < 0$.

In Eq. (9), $\delta_e = \beta\delta_t$ if $\delta_n < 0$ due to the fact that the contact of the crack surfaces is treated as phenomena independent of the actual cohesive model, which is similar to how Camacho and Ortiz (1996) and Ortiz and Pandolfi (1999) treated it. When the crack is closed, the contact forces between the contacting crack surfaces are solved, as presented in Section 2.1 for the blocks. Hence, in the case of relative sliding of the closed crack surfaces under compression, the cohesive crack growth is simultaneously resisted by both the frictional and cohesive forces. Due to this, the friction coefficient μ was included in the failure criterion through the definition of t_e on the compressive side (see Eqs. (5) and (6)): If μ is not included in the failure criterion and the failure initiated under compression with $|t_t| = \tau_{cr}$, then the cohesive crack growth would be arrested by friction until $|t_t| > \mu|t_n|$.

The cohesive crack growth can include loading, unloading and reloading phases, as illustrated in Fig. 4: in loading phase δ_e increases, in unloading it decreases, and in reloading again increases but has a value smaller than maximum effective crack opening displacement δ_m reached in preceding loading phase. The irreversibility of this crack growth process is ensured by solving the cohesive force value during these phases based on

$$|\mathbf{f}_c|(\delta_e) = \begin{cases} \left|\mathbf{f}_c^0\right|\left(1 - \dfrac{\delta_e}{\delta_f}\right) & \text{for loading} \\ \left|\mathbf{f}_c^0\right|\left(1 - \dfrac{\delta_m}{\delta_f}\right)\dfrac{\delta_e}{\delta_m} & \text{for un}-\text{/reloading.} \end{cases} \tag{10}$$

The direction of the cohesive force depends on components δ_t and δ_n of cohesive crack opening displacement δ. When using these components, the tangential and normal components of the cohesive force are, respectively, solved from the following equation:

$$f_{ct} = |\mathbf{f}_c|(\delta_e)\left(\frac{\beta\delta_t}{\delta_e}\right) \quad \text{and} \quad f_{cn} = |\mathbf{f}_c|(\delta_e)\left(\frac{\langle\delta_n\rangle}{\delta_e}\right). \tag{11}$$

As Fig. 4 further shows, $|\mathbf{f}_c(\delta_e)|$ linearly decreases with an increasing δ_e and vanishes once δ_e reaches δ_f. The value of δ_f is not a material parameter, but instead is derived from the fracture energy G: If the length of the newly formed crack surfaces associated with a bond point is l, the energy dissipated due to the cohesive crack growth process at the point should be equal to Gl in 2D. When using the definition for work, linear softening law in Fig. 4, and requiring the dissipation in the cohesive crack growth to be equal to Gl, the value of δ_f is achieved from

$$\int_0^{\delta_f} |\mathbf{f}_c(\delta_e)|\,d\delta = \frac{1}{2}\left|\mathbf{f}_c^0\right|\delta_f = Gl \quad \Rightarrow \quad \delta_f = \frac{2Gl}{\left|\mathbf{f}_c^0\right|}. \tag{12}$$

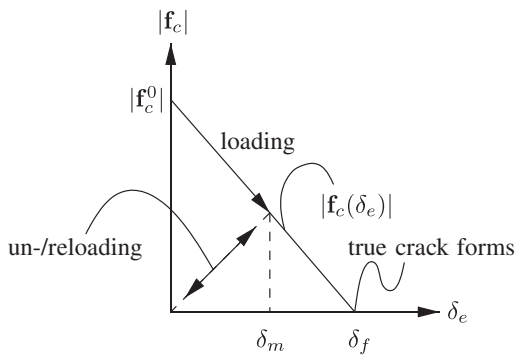

Fig. 4. Linear softening function $\mathbf{f}_c(\delta_e)$ and the crack opening, unloading and reloading phases of the cohesive crack growth. In the figure, δ_e is the effective crack opening displacement defined in Eq. (9), δ_m is the maximum crack opening displacement achieved during the loading phase, and δ_f is the critical crack opening displacement.

2.4. Virtual punch through experiments

The simulations were performed in two phases: (1) During the initial phase the initial configuration of the rubble was generated and (2) during the punch through phase the indentor penetrated the rubble. The first phase was performed using rigid blocks in a manner similar to that of Polojärvi and Tuhkuri (2009) and Polojärvi et al. (2012) to achieve different initial configurations for the ridges. During the first phase, the rigid blocks were released under water with random orientations and velocities and allowed to float until their kinetic energy had dissipated, and a quasi-static rubble pile had formed. At the end of the first phase, the rubble pile was meshed using Gmsh finite element mesh generator (Geuzaine and Remacle, 2009) for the second phase of the simulation.

At the beginning of the second phase, the buoyant force and gravitation were applied to the whole rubble mass, consolidated layer, and indentor platen. The buoyant force acting on the indentor platen was subtracted from the indentor force records. Before any indentor motion, it was ensured that the system was in balance. The boundary conditions and the simulation domain for the punch through phase of the simulations are illustrated in Fig. 5, with the values for the dimensions in the figure shown in Table 1. The domain width w was 50 m. The simulations showed that the domain was substantially wider than the width of the area of moving rubble during indentor penetration.

The block dimensions were randomly varied within each simulated ridge so that the block thickness and length varied between 0.2 and 0.4 m and 0.6 and 1.8 m, respectively, with the lower bound for thickness chosen based on Heinonen (2004). This random generation of the blocks resulted into aspect ratio distribution with a mean at ~1:3.5. The ridge keel thickness, h, and the consolidated layer thickness given in Table 1 were chosen after full scale punch through experiments reported and analysed by (Heinonen, 2004). In his experiments, rubble thicknesses varied between 2.2 and 5 m (mean value 3.8 m), with consolidated layer thickness varying between 0.6 and 1.4 m (mean value 1 m). The rubble was freeze bonded to the consolidated layer. The indentor width, $w_I = 4$ m, used here was always at least ten times higher than the block thickness, similarly

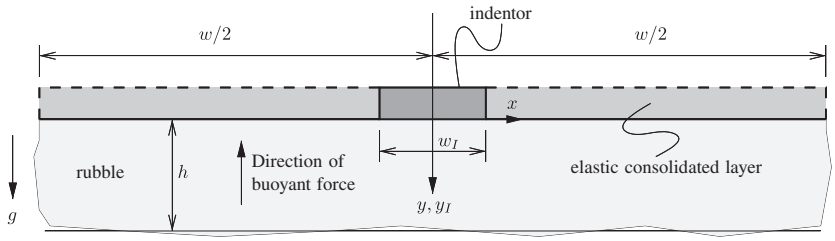

Fig. 5. Simulation domain and boundary conditions. The upper boundaries of the consolidated layer (marked with dashed lines) had a rigid boundary condition. The symbols in the figure are as follows: h is the rubble thickness, w the domain width, y_I the direction of indentor penetration, and g the gravitational acceleration. The values of the dimensions in the figure are collected in Table 1. The axes (x, y) of the global coordinate system are also shown in the figure.

to the experiments by Heinonen (2004). The consolidated layer and the indentor were elastic. For simplicity, the material parameters for the consolidated layer and the indentor were the same as for the rubble blocks.

The freeze bond strength was not constant through the rubble depth but instead decreased linearly towards the bottom of the rubble, where the bond shear and tensile strength values were ~10% of those on the top. Simple linear relation was used, as experimental data indicates, that the layer of partially consolidated rubble does not necessarily reach through the rubble thickness (Croasdale et al., 2001; Høyland and Løset, 1999; Leppäranta and Hakala, 1989, 1992; Timco et al., 2000).

A number of freeze bond strength values were used in the simulations. As Table 1 shows, the freeze bond shear strength on top of the rubble τ_{cr} varied between 5 and 100 kPa. The lowest τ_{cr} values used are close to those measured in a laboratory (Ettema and Schaefer, 1986; Repetto-Llamazares et al., 2011a,2011b), while the higher ones are close to those measured in field studies (Shafrova and Høyland, 2008) or achieved by a rough scaling of the laboratory experiments (Ettema and Schaefer, 1986; Liferov, 2005). Unfortunately there is a lack of data on the freeze bond tensile strengths (σ_{cr}), hence 10 kPa on top of the rubble was used here.

Table 1
Main parameters and dimensions used in the simulations. The directions (Dir.) given in the table refer to the global coordinate system in Fig. 5. Since the freeze bond shear strength linearly decreased towards the bottom of the pile, the value in the table refers to the value on top of the rubble.

	Parameter	Dir.	Symbol	Unit	Value
General	number of blocks	–	–	–	665
	gravitational acceleration	–	g	ms^{-2}	9.81
	domain width	–	–	m	50
	ndof	–	–	–	~150,000
Contact	penalty term	–	s	–	2×10^{11}
	time step	–	Δt	s	$1\times10^{(-6)}$
Blocks	length	–	–	m	0.6–1.8
	thickness	–	–	m	0.2–0.4
	mass density	–	ρ_b	kg m^{-3}	920
	friction coefficient	–	μ	–	0.05, 0.3
	Young's modulus	–	E	GPa	2
	viscous damping constant	–	–	Pas	2.5×10^{4}
Water	mass density	–	ρ_w	kg m^{-3}	1010
Rubble	keel depth	–	h	m	~4
	bulk porosity	–	η	–	~0.25
Indentor	width	x	w_I	m	4
	thickness	y	h_I	m	1
	final velocity	y	v_I	ms^{-1}	0.1
Consolidated layer	thickness	y	–	m	1
	Young's modulus	–	–	GPa	2
Freeze bond	Shear strength	–	τ_{cr}	kPa	5…100
	Tensile strength	–	σ_{cr}	kPa	10
	Fracture energy	–	G	Jm^{-2}	15

Furthermore Table 1 shows the elastic modulus, $E=2$ GPa, used in the simulations; it was chosen based on the values 1 to 5 GPa for the strain modulus of first-year sea ice suggested by Timco and Weeks (2010). The friction coefficient values $\mu=0.05$ and 0.3 were used based on values $\mu\approx0.02-0.7$, which are reported in the literature for ice (Frederking and Barker, 2002; Lishman et al., 2009; Pritchard et al., 2011). Fracture energy for the freeze bonds, $G=15$ Jm $^{-2}$, was chosen after that of the first-year sea ice (Dempsey et al., 1999). Similar to the freeze bond strength, G decreased linearly towards the bottom of the rubble. Porosity η, which defines the ratio between the area of the voids and the area of solid material within the rubble, was measured in the initial rubble configuration. Hence, η was not predetermined, but, instead, was a result of the first simulation phase described above.

The indentor motion was displacement driven, with the displacement being controlled on top of the indentor platen. The indentor was accelerated to its final velocity of 0.1 ms^{-1} during the first two seconds of its motion to avoid a load due to inertia of the rubble. A number of simulations with various slower indentor velocities were used to verify, that a peak load that appeared at the beginning of the indentor penetration was not due to the inertia of the rubble pile, but, instead, due to its quasi-static response. Lowering the indentor velocity to 0.01 ms^{-1} while keeping the acceleration time constant decreased the load at the initial peak by only 3%, hence it was concluded that the indentor force was virtually only due to static load.

3. Results and analysis

We performed the simulations on four different ridge geometries, hereafter referred to as Ridges 1–4, which had been generated during phase 1 of the simulations (see Section 2.4). We used various freeze bond strengths and two friction coefficients for the simulations. In all the simulations, the strength of the freeze bonds decreased linearly towards the bottom of the rubble, as described in Section 2.4. For brevity, this is not mentioned in the text below and all of the freeze bond strength values provided refer to their maximum values on top of the rubble. As we ran the simulations in 2D, the force values presented below are per unit width.

3.1. Force-displacement records and maximum indentor force

We observed that the freeze bond strength, friction coefficient, and ridge geometry all affected the force-displacement ($F-y_I$) records and load levels. In the following section we first present the effect of ridge geometry on the $F-y_I$ records and load levels. Then, we describe the effect of freeze bond strength on the $F-y_I$ records and load levels.

3.1.1. Force records and ridge geometries

The typical features observed in the simulations can be described using the force-displacement ($F-y_I$) records from the simulations performed on Ridges 1 and 3 shown in Fig. 6a and b. The $F-y_I$ records

in the figures are from the simulations which were performed with a freeze bond shear and tensile strength of $\tau_{cr}=50$ kPa and $\sigma_{cr}=10$ kPa, respectively, and with friction coefficients of $\mu=0.05$ and 0.3. For more detail, Fig. 7a and b show close-ups of both the $F-y_I$ records in Fig. 6a and b from the beginning of the indentor penetration.

As Figs. 6 and 7 illustrate, F initially increased with a high rate, $\partial F/\partial y_I$, due to rubble buoyancy and system stiffness. The friction coefficient μ had virtually no effect on the rate, $\partial F/\partial y_I$, during the initial increase in F, as shown by Fig. 7. Following the steep increase in F, the simulations yielded a cohesive peak load F^m, which corresponded to the onset of the freeze bond failures within the rubble. This peak load, F^m, was also the maximum load in the simulations.

A comparison of Fig. 7a and b already suggests that the value of F^m was significantly affected by the ridge geometry (the different block arrangements generated during the first simulation phase, described in Section 2.4), whereas with these bond strength parameters ($\tau_{cr}=50$ kPa and $\sigma_{cr}=10$) the friction coefficient μ did not have a major effect on the load. This can clearly be seen from the F^m values from the simulations for Ridges 1–4 with the values $\tau_{cr}=50$ kPa and $\sigma_{cr}=10$ kPa

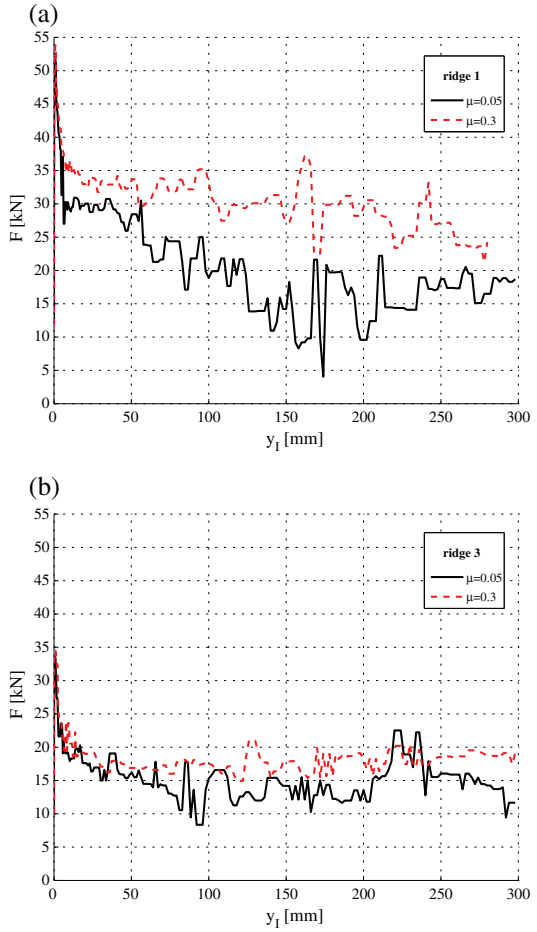

Fig. 6. Indentor force-displacement ($F-y_I$) records from simulations of Ridge 1 and 3, which yielded maximum and minimum peak force F^m values with a friction coefficient $\mu=0.05$ and $\mu=0.3$. In both of the simulations shown here, the freeze bond shear and tensile strengths were $\tau_{cr}=50$ kPa and $\sigma_{cr}=10$ kPa, respectively. The values of F^m for all ridges are given Fig. 10.

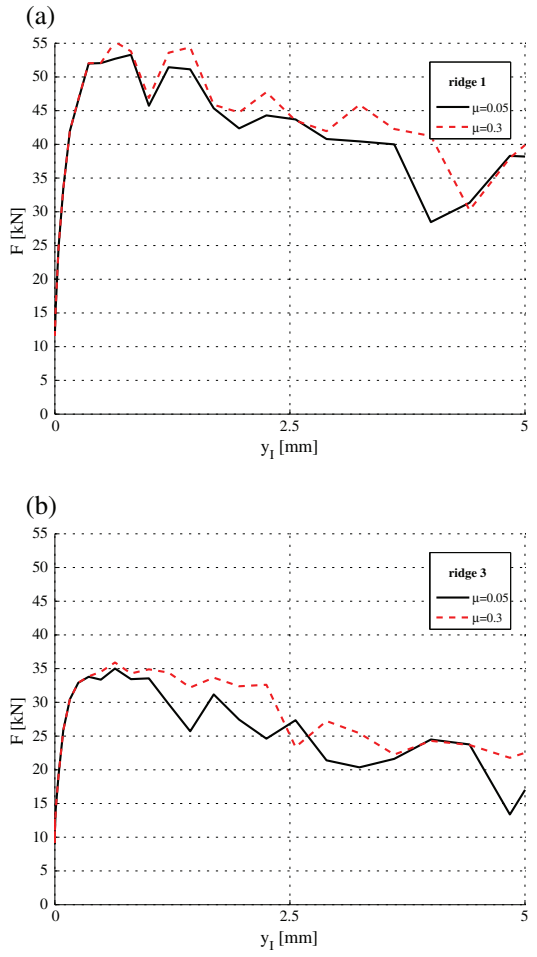

Fig. 7. Close-ups of the indentor force-displacement ($F-y_I$) records from the simulations of Ridges 1 and 3 given in Fig. 6. The data in the close-ups covers the initial increase and the peak load, F^m.

given in Fig. 8. The data in Fig. 8 clearly shows that the difference in F^m yielded by the different ridges with constant μ was up to ~50%. On the other hand, the difference in the F^m due to μ was only 2–7% depending on the ridge.

After the peak load F^m, with increasing indentor penetration y_I, F decreased steeply as Fig. 6a and b show. During the steep decrease, the freeze bonds failed through the rubble thickness, that is, the decrease in F was due to a global failure of the rubble freeze bonds. In this global failure, the majority of the failing bonds lay on distinct zones around the indentor perimeter. A failure plane could be defined through these zones, as described in the next section. The steep decrease in F lasted up to $y_I\approx20$ mm of indentor penetration.

As the $F-y_I$ records in Fig. 6a and b further illustrate, the post-peak load after the steep decrease in F from F^m was depended not only on the ridge geometry, but also on the friction coefficient μ. With the friction coefficient $\mu=0.05$, the load typically decreased up to an indentor penetration of $y_I=50\ldots150$ mm, whereas with the friction coefficient $\mu=0.3$ the decrease was either very slow (Ridge 1 in Fig. 6a) or virtually nonexistent (Ridge 3 in Fig. 6b). The value of F^m with the value $\mu=0.05$ ($\mu=0.3$) for each ridge was between

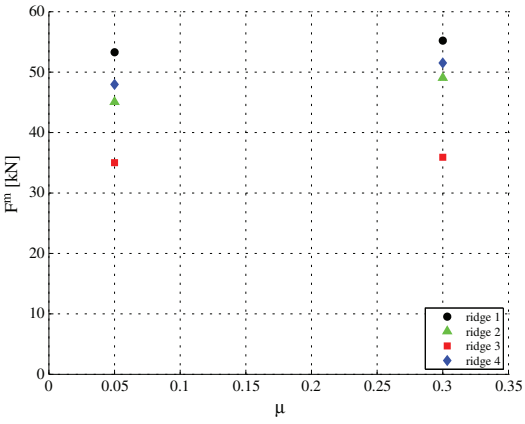

Fig. 8. The maximum load F^m as a function of μ for four different ridges. Whereas the friction coefficient only had a negligible effect on the F^m, the different initial configurations resulted as much as ~50% difference in the F^m. The freeze bond shear and tensile strengths on top of the rubble were $\tau_{cr}=50$ kPa and $\sigma_{cr}=10$ kPa, respectively, for all ridges.

2.0 and 3.2 (1.9 and 2.6) times higher, than the mean load for the penetration interval $y_l=150…300$ mm for simulations with the bond strength values $\sigma_{cr}=10$ kPa and $\tau_{cr}=50$ kPa.

3.1.2. Force records and freeze bond strength

The freeze bond shear strength, τ_{cr}, affected the indentor force-displacement ($F-y_l$) records most clearly during the cohesive peak at the beginning of the indentor penetration. The effect of τ_{cr} on the cohesive peak is illustrated by Fig. 9, which shows the $F-y_l$ records from the beginning of the simulated indentor penetration on Ridge 1 with τ_{cr} equal to 5, 12.5, 25 and 50 kPa. Besides the beginning, the $F-y_l$ records with all τ_{cr} showed features similar to those described above.

The peak load F^m values increased with τ_{cr}, as shown in Fig. 10. As the figure illustrates, the rate $\partial F^m/\partial\tau_{cr}$ was not constant, but in general it was somewhat higher with low rather than with high τ_{cr} values. The change in the rate $\partial F^m/\partial\tau_{cr}$ when using different τ_{cr} values was explained by the relation of the rubble deformation patterns and τ_{cr} as shown in the next section.

Furthermore, Fig. 10 suggests, that an increase in μ increased the F^m more in the case of weakly bonded ridges, rather than strongly bonded ridges. This is clearly shown by the ratios of the F^m values from the simulations with μ being equal to 0.3 and 0.05 for Ridges 1–4 given in Fig. 11. As the figure shows, the effect of μ on the F^m values depended on the geometry of the ridge, but decreased as the τ_{cr} was increased. In the case of loosely bonded ridges, μ increased the maximum load by up to 28%. On the other hand, with the highest value of τ_{cr} used here, the effect of μ on the value of F^m was negligible (~2.5%).

3.2. Failure process and rubble deformation

The failure process and deformation patterns were related to the maximum force, F^m, and the post peak indentor load, F, levels. In general, the ridges yielding the highest indentor load values had the highest amount of rubble mass displacing due to initial global failure. Furthermore, the post-peak indentor load records depended on the rubble mass displacing, not only directly under the indentor but also outside the perimeter of the indentor. The analysis in this section is divided into two parts: first we study F^m using the initial failure planes within the rubble, after which we analyze the post-peak load levels using the deformation patterns.

3.2.1. Failure planes and maximum load

The effects of ridge geometry and freeze bond shear strength on the maximum load, F^m, were related to differences in the initial failure planes within the rubble. The initial failure planes affected the amount of rubble mass supported by the indentor and the load component due to rubble buoyancy. We assessed the initial rubble failure using angle α of the rubble failure planes, defined in Fig. 12.

To define α, we collected the positions of the failed freeze bond points at some instant from the simulation data (Fig. 12). Then, we used the least squares method to determine two linear fits: One for the failures with $x<-w_l/2$ (with w_l being the indentor width) and another for failures with $x>w_l/2$. The values for α for $x<-w_l/2$ and $x>w_l/2$ were then obtained from the angles of the linear fits in relation to the vertical with the positive direction being away from the center line of the indentor (see Fig. 12). It should be noted, that the

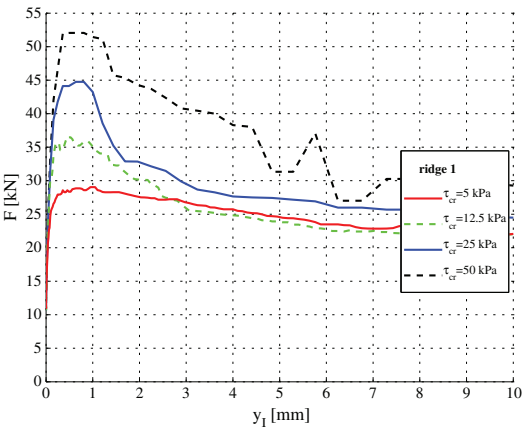

Fig. 9. Indentor force-displacement ($F-y_l$) records from the beginning of the indentor penetration showing the effect of freeze bond shear strength τ_{cr} on peak load. In all of the simulations shown here, the friction coefficient $\mu=0.05$ and freeze bond tensile strength $\sigma_{cr}=10$ kPa.

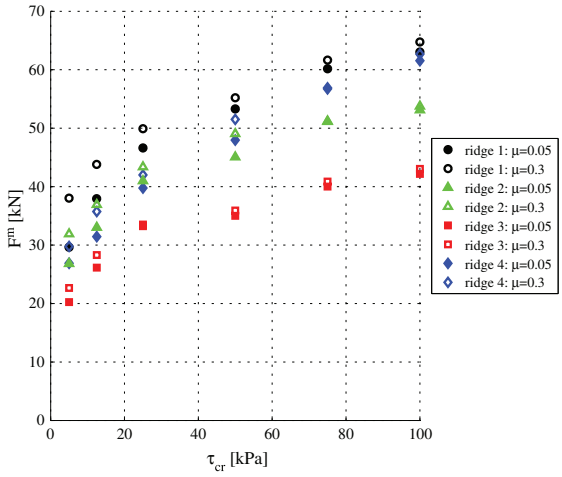

Fig. 10. The maximum load, F^m, as a function of the critical freeze bond shear strength, τ_{cr}. The marker fill color in the figure indicates the F^m values from the simulations with different friction coefficients μ as shown by the legend.

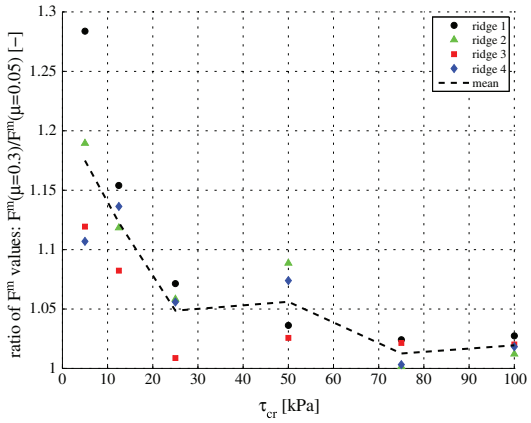

Fig. 11. Ratio of the maximum load F^m values from simulations with friction coefficient values of 0.05 and 0.3 as a function of freeze bond shear strength τ_{cr}. In addition, the figure shows the mean ratio for all the data. All of the simulations with the data shown in the figure had a freeze bond tensile strength $\sigma_{cr}=10$ kPa.

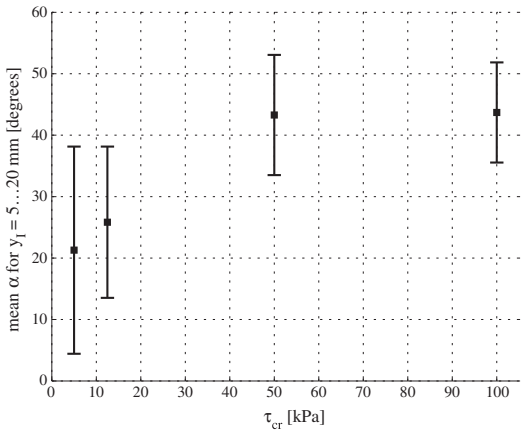

Fig. 13. The mean values of the failure plane angles $\bar{\alpha}$ for the indentor displacement interval $y_I=1\ldots20$ mm as a function of freeze bond shear strength τ_{cr}. The data is from simulations done for Ridges 1–4 with friction coefficient values $\mu=0.05$ and 0.3 and freeze bond tensile strength $\sigma_{cr}=10$ kPa.

failure planes, as they are defined here, were not constrained to align with the indentor platen corners. Angle α described the initial rubble failure fairly well, but it should not be used for large indentor displacements when the zones for failed freeze bonds became less distinct.

The α values showed a similar increase with freeze bond shear strength τ_{cr} as the peak load, F^m, in Fig. 10: α increased with τ_{cr} up to 50 kPa; after that, it remained fairly constant. This increase in α is shown in Fig. 13, which gives the mean values of α with their standard deviations as a function of τ_{cr}. The data from all of the simulations with the indentor displacement interval $y_I=1\ldots20$ mm are included in the figure. The displacement interval was chosen so, that all of the simulations had advanced to a point after the steep decrease in F following the initial cohesive peak. As the standard deviations in the figure indicate, α showed relatively wide scatter. The friction coefficient μ had a negligible effect on α; for example, simulations with $\tau_{cr}=50$ kPa yielded mean α values of $43\pm8°$ and $44\pm7°$ with $\mu=0.05$ and $\mu=0.3$, respectively.

To study the initial rubble failure patterns, the linear fits used to determine α were further used to define the area, A_p, of the plug that formed during the initial rubble failure (see Fig. 12). The A_p is limited by the linear fits used to define the angle α and the lines passing the uppermost and lowermost failed bond on each side of the indentor. Fig. 14 gives the mean A_p values for a indentor penetration interval $y_I=1\ldots20$ mm for each ridge (Fig. 14a) and the mean for all of the ridges (Fig. 14b) with different friction coefficient μ values. As Fig. 14b shows, μ only slightly affected the initial rubble failure patterns.

The A_p values in Fig. 14a and b clearly suggest that the increase in freeze bond strength induces a change in the initial rubble failure patterns up to a certain strength (here up to $\tau_{cr}=50$ kPa), with no change in the failure patterns when the freeze bond strengths are increased further. The change in the rate $\partial A_p/\partial\tau_{cr}$ with low τ_{cr} values is likely related to the change in the rate $\partial F^m/\partial\tau_{cr}$, which occurs around same freeze bond strength values (see Section 3.1.2 and Fig. 10). Hence, high $\partial F^m/\partial\tau_{cr}$ with a low τ_{cr} is due to changes in both, the rubble strength and the initial failure patterns, whereas with a high τ_{cr}, the $\partial F^m/\partial\tau_{cr}$ is only due to an increase in the rubble strength.

The initial plug areas, A_p, were further used to derive the buoyant load, F_b, resulting the plug in order to compare the buoyant force and load levels. From the A_p values, and the porosities η of each ridge, we calculated the F_b using the following equation:

$$F_b\left(A_p,\eta\right)=(1-\eta)(\rho_w-\rho_i)gA_p, \tag{13}$$

where ρ_w and ρ_i are the mass densities of water and ice, respectively, and g is the gravitational acceleration.

The values for $F_b(A_p,\eta)$ are shown in Fig. 15 at an indentor penetration $y_I=20$ mm, together with F^m and the load F at $y_I=20$ mm, as function of A_p for Ridges 1–4 with $\tau_{cr}=50$ kPa. Hence, the figure

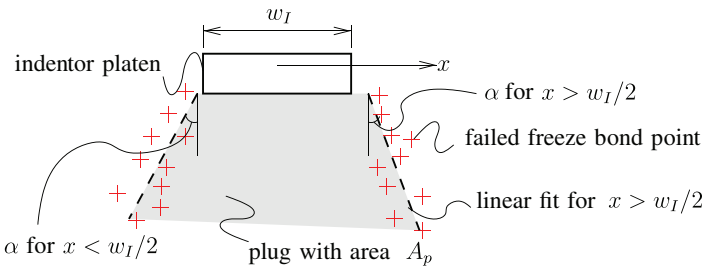

Fig. 12. Derivation of the angle α of failure planes using failed freeze bond points (red crosses), the least squares method and the linear fits (dashed lines). The positive direction of α is away from the center line of the indentor on both sides of the indentor. In addition, the figure shows the area, A_p, of a rubble plug forming under the indentor as a result of the failure (gray), defined here as a four-sided polygon with two edges aligned with the linear fits.

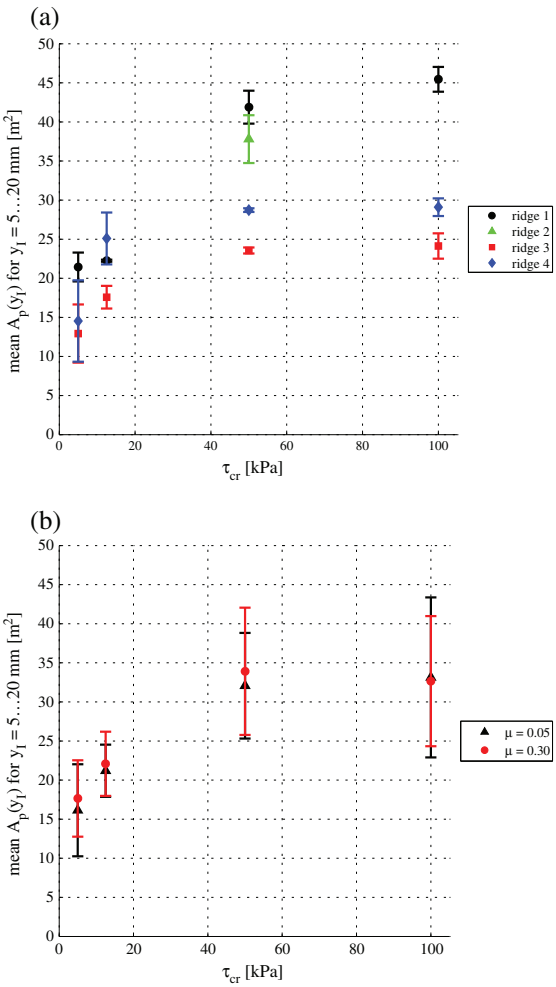

Fig. 14. Mean areas, A_p, of the plug forming in the initial failure (see Fig. 12) during indentor displacement interval of $y_I = 1...20$ mm as a function of freeze bond shear strength τ_{cr}: (a) Shows the data for each ridge and (b) shows the mean values of the data for different friction coefficients, μ. The data is from simulations of Ridges 1–4 with a freeze bond tensile strength $\sigma_{cr} = 10$ kPa. For the discussion provided in Section 4.1.1, it should be noticed that the rubble area directly under the indentor in all experiments was ~16 m^2.

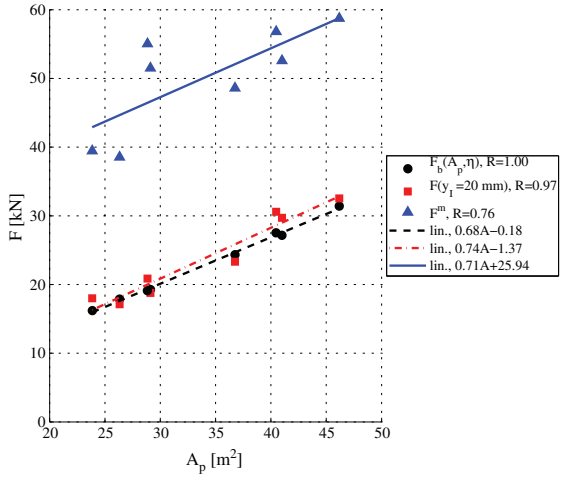

Fig. 15. Force values as a function of the area, A_p (see Fig. 12), of the rubble plug formed under the indentor at indentor penetration of $y_I = 20$ mm: Maximum load F^m, the load F when $y_I = 20$ mm, and the buoyant load $F_b(A_p,\eta)$ of the plug (see Eq. (13)). The figure shows data from the simulations of Ridges 1–4 with the friction coefficients $\mu = 0.05$ and $\mu = 0.3$. For all of the simulations, the freeze bond shear and tensile strengths were $u_{cr} = 50$ kPa and $\sigma_{cr} = 10$ kPa, respectively.

illustrates the effect of the ridge geometry on the F^m and the difference in the buoyant load component included in F^m between ridges.

The three main observations illustrated by Fig. 15 are as follows: (1) the F^m is very likely influenced by the buoyant load $F_b(A_p,\eta)$ of the plug, (2) the $F_b(A_p,\eta)$ is different for different ridges, and (3) after the cohesive peak, the load is due to buoyancy of the rubble plug separating from the rest of the rubble. These observations are shown by the fact that the F^m and $F(y_I = 20$ mm) values in the figure increase with A_p, with only a slight difference between the rates $\partial F^m/\partial A_p$, $\partial F(y_I = 20$ mm)$/\partial A_p$, and $\partial F_b(A_p,\eta)/\partial A_p$. Hence, F^m and $F(y_I = 20$ mm) are likely both related to A_p and thus related on the buoyant force $F_b(A_p,\eta)$ due to the plug.

Since the data from all four ridges is included in Fig. 15, the difference in the F^m due to ridge geometry is likely related to the difference in the buoyant load due to the rubble plug. From Fig. 15 it should be noticed, that $F_b(A_p,\eta)$ and F^m show similar behavior with A_p and that the $F_b(A_p,\eta)$ values are ~50% of the F^m values. These observations indicate, that F^m values likely include a considerable buoyant component, which should be taken into account when interpreting the $F-y_I$ records, as will be discussed in Section 4.1.1.

3.2.2. Deformation patterns and post-peak load

The post-peak indentor load was related to the rubble deformation patterns. The deformation patterns depended on the ridge geometry as illustrated in Fig. 16. The figure shows the vertical displacement field u_y of the rubble at an indentor penetration of $y_I = 5$ mm.

The deformation patterns of Ridges 1 and 3, which are shown in Fig. 16 are clearly different: The area of the rubble mass moving downwards is significantly larger on Ridge 1 than on Ridge 3. Correspondingly, the indentor load for Ridge 1 was ~50% higher than for Ridge 3 around $y_I = 5$ mm (see Figs. 6–8). For the following discussion, we should note, that the area of rubble having the same displacement as the indentor ($y_I = 5$ mm, indicated by darkest blue in the figure), was approximately equal for Ridges 1 and 3.

In order to show the relationship between the observations of the previous paragraph and the post peak indentor load, we defined the areas of the displaced rubble as illustrated by Fig. 17. At various indentor displacements, y_I, we used downward rubble displacement fields, u_y (illustrated by the colors in Fig. 16) to define areas A_d of the rubble displaced by more than some ratio $K = \{0...1\}$ of y_I. Hence, $A_d = A_d(K,y_I)$ and, for example, the area $A_d(K = 0.5,\ y_I = 100$ mm) includes rubble with $u_y > 0.5 \times 100$ mm $= 50$ mm. Similarly to the previous section, the areas, $A_d(K,y_I)$, were also used to derive a buoyant load

$$F_d(K,y_I) = (1-\eta)(\rho_w - \rho_i) g A_d(K,y_I), \tag{14}$$

which can be compared with the post-peak indentor load. As an example, the load $F_d(K = 0.5, y_I = 100$ mm) is an estimate for buoyant load of rubble with $u_y \geq 50$ mm.

An example of the results of the analysis described above in Fig. 18 demonstrates the effect of rubble deformation patterns on the post-peak indentor load, and it shows that a mass larger than just the rubble directly under the indentor likely contributed to the buoyant load component included in F. Fig. 18 shows the $F(y_I)$, $F_d(K = 0.45, y_I)$

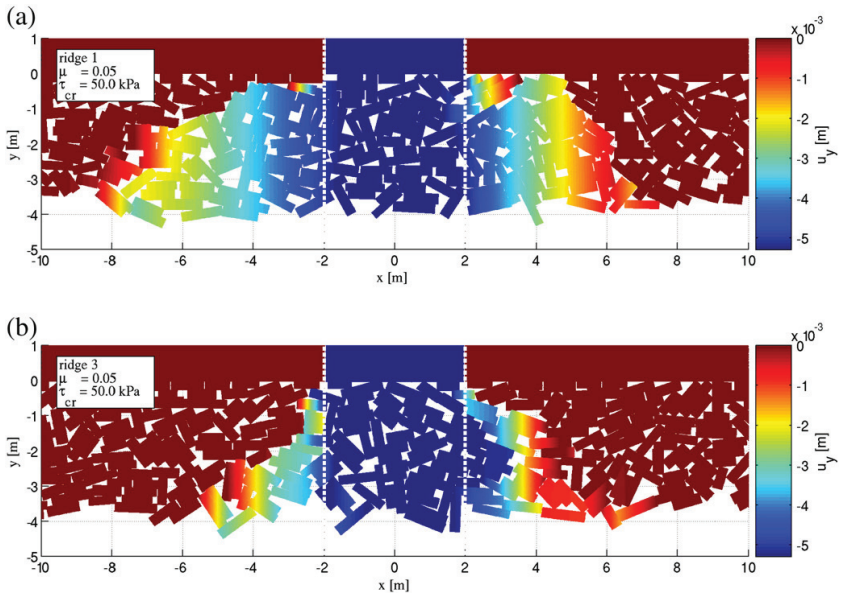

Fig. 16. Rubble deformation patterns for Ridges (a) 1 and (b) 3 after an indentor penetration of $y_I = 5$ mm. The colors indicate vertical displacement u_y. In both simulations, $\tau_{cr} = 50$ kPa, $\sigma_{cr} = 10$ kPa, and $\mu = 0.05$. The figures show part $-10\ \text{m} \le x \le 10\ \text{m}$ of the domain. The indentor perimeter in the x-direction is indicated by thick white dashed lines.

and $F_d(K = 0.9, y_I)$ graphs from a simulation done on Ridge 1 plotted against the indentor displacements.

The three plots in Fig. 18 depict the change in the rubble deformation field with displacement, which can also be seen by comparing Figs. 16a and 19: The rubble plug that started to move after the initial failure (Fig. 16a) dissolved due to freeze bond failures during the indentor penetration, which led to a smaller amount of rubble moving downwards later in the simulation (Fig. 19). Corresponding to this change in rubble deformation field, F and $F_d(K = 0.45, y_I)$ in Fig. 18 both decreased with increasing y_I. Furthermore Figs. 16a and 19 show, that the amount of rubble that moved the same amount as the indentor (dark blue area in the figures) remained approximately constant, which explains the smaller decrease in $F_d(K = 0.9, y_I)$ in Fig. 18. It should be noted, that the value $F_d(K = 0.45, y_I)$ in Fig. 18 cannot be the exact buoyant component of F because at certain instants $F_d(K = 0.45, y_I) > F$; rather, it is merely an estimate of the buoyant component and how it changes.

A similar relationship between the deformation fields and the post-peak load levels applied for all simulations. To show this, we derived data sets with values of $A_d(K, y_I)$ with $K = \{0.1, 0.45, 0.9\}$ and $y_I = \{20, 30, 40, \ldots, 150\}$ mm and corresponding F values for each simulation. One such set would include the $F_d(K, y_I)$ and F data given by the markers in Fig. 18. The $F - A_d(K, y_I)$ sets from all of the simulations for each $K = \{0.1, 0.45, 0.9\}$ are shown in Fig. 20a and b, together with their correlation coefficients (R) and linear fits. Fig. 20a gives $F - A_d$ data from the simulations done on Ridges 1–4 with freeze bond shear and tensile strengths of $\tau_{cr} = 50$ kPa and $\sigma_{cr} = 10$ kPa, respectively, and Fig. 20b includes the data from all of the simulations. In both figures the data from simulations with the values $\mu = 0.05$ and $\mu = 0.3$ are included. In addition, the figures show a line for buoyant force $F = (1 - \bar{\eta})(\rho_w - \rho_i) g A$, where $\bar{\eta}$ is the mean porosity of Ridges 1–4.

Figs. 18 and 20 illustrate three important findings related to the interpretation of punch through test $F - y_I$ records on the post-peak regime: (1) The assumption, that only the rubble directly under the

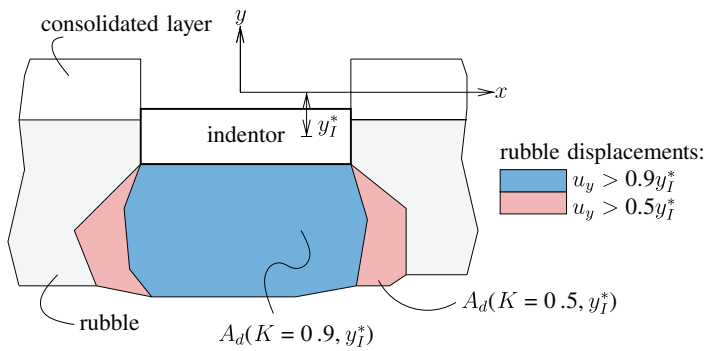

Fig. 17. Definition of $A_d(K, y_I)$ for K values of 0.5 and 0.9: As shown in the illustration, for example the $A_d(K = 0.5, y_I^*)$ at indentor displacement y_I^* includes the rubble with downward displacements of $u_y > 0.5 y_I^*$.

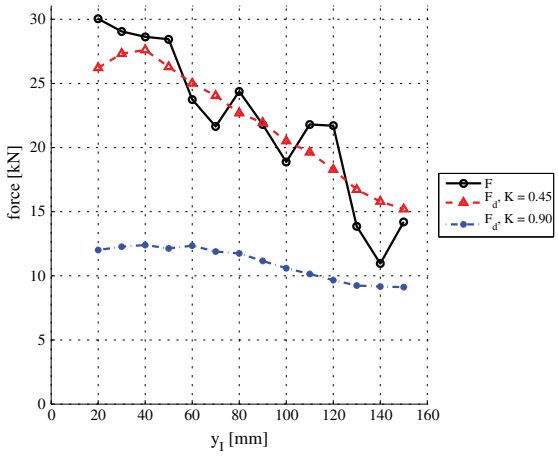

Fig. 18. Post-peak indentor load F (black line) as a function of the indentor penetration $y_I = \{20,30,40, \ldots,150\}$ mm from a simulation done on Ridge 1 with the buoyant forces $F_d(K=0.45)$ (dashed red line) and $F_d(K=0.9)$ (dash dotted blue line) given by Eq. (14). In the simulation, the friction coefficient μ was 0.05, and the freeze bond shear (τ_{cr}) and tensile strengths (σ_{cr}) were 50 kPa and 10 kPa, respectively.

indentor causes the buoyant load component is incorrect, as (2) the indentor supports a larger volume of displacing rubble, leading to (3) the post-peak load having a large component due to buoyancy, which can decrease and be mistaken for as material softening.

The first two findings in the previous paragraph are shown by the correlation coefficients, R, for the data sets $F-A_d(K,y_I)$ in Fig. 20. These are $R=0.13$ when $K=0.9$ (no correlation) and $R=0.88$ when $K=0.45$ (clear correlation) for the different ridge geometries with constant freeze bond properties (Fig. 20a). For all of the simulations, data set $F-A_d(K=0.9, y_I)$ shown had the value $R=0.46$, but still data set $F-A_d(K=0.45, y_I)$ with the value $R=0.82$ clearly yield the best correlation (Fig. 20b). The data set $F-A_d(K=0.9, y_I)$ show better correlation in Fig. 20b than in Fig. 20a, which was due to higher $A_d(K=0.9, y_I)$ values for the highest freeze bond strengths ($\tau_{cr}=100$ kPa).

In addition to the R values, the lines giving the buoyant load as a function of A in Fig. 20a and b support the second finding in both cases, since the data set $F-A_d(K=0.45, y_I)$ data points in general lie close to the lines in the figures. The last finding is also supported by the data set $F-A_d(K=0.45, y_I)$ in Fig. 20a and b, and was also illustrated by Fig. 18: A decrease in $A_d(K=0.45, y_I)$ leads to a decrease in the post-peak F. Hence, the decrease in F is related to a change in the deformation patterns of the rubble pile, not to the softening of the rubble material itself.

4. Discussion

4.1. Rubble shear strength and material modeling

In the following section, we discuss the interpretation of the punch through experiment results based on the results presented in the previous section. First we discuss the derivation of the rubble shear strength, τ, and consider the effect of incorrect assessment of the buoyant load component. We demonstrate that an incorrect estimate for the buoyant indentor load component has a major effect on τ values derived for rubble after punch through experiment results. Then, we discuss how the rubble friction angle is estimated, and we argue that the punch through experiments may not be a suitable method for deriving a friction angle for ice rubble. This is due to the fact that the tensile freeze bond failures dominate the rubble failure process.

4.1.1. Shear strength of the rubble

To derive τ for the rubble, it is necessary to make assumptions about the rubble failure process and failure patterns. Usually as a first assumption, the failure is assumed to occur on the vertical planes that are aligned with the indentor perimeter and reach through the rubble (Croasdale et al., 2001; Heinonen, 2004; Serré, 2011). In 3D with a round indentor, this assumption leads to a so-called cylindrical failure. For brevity, the term cylindrical failure is subsequently applied to a 2D failure with failure planes that are aligned with the indentor corners and have angle $\alpha=0$ in relation to the vertical (see Fig. 12).

The rubble shear strength, τ, is often derived using the maximum indentor load, F^m, and is assumed to be given by the following equation (Azarnejad and Brown, 2001; Leppäranta and Hakala, 1992):

$$\tau = \frac{F^m - F_b}{A_s}, \tag{15}$$

where F_b is the buoyant component of the indentor load and A_s is the area of the shear planes within the rubble. For the following analysis, we chose the A_s after cylindrical failure in 2D, thus $A_s=2h$ (with h being the rubble thickness).

In earlier studies, different estimates for the buoyant load component, F^b, in Eq. (15) has been used. Here, we consider three options: (1) Only taking account the maximum load F^m ($F^b=0$), as in, for example Heinonen (2004), Croasdale et al. (2001) and Serré (2011); (2) assuming that the buoyant load is a result of a cylindrical plug ($F_b \approx 11$ kPa for all simulations here), as in, for example Leppäranta and Hakala (1992), and (3) using the formula $F^b=F_b(A_p,\eta)$ from Eq. (13), assuming that the buoyant load is a result of a plug forming in the initial failure (see Fig. 12). As in the case of Fig. 15, $F_b(A_p,\eta)$ at the instant of the indentor displacement $y_I=20$ mm is used in the following.

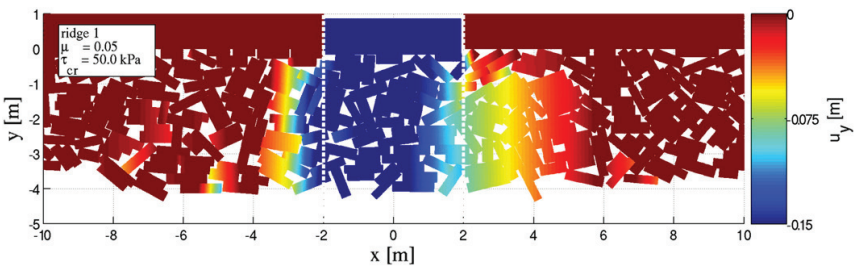

Fig. 19. Downward rubble displacements of Ridge 1 at an indentor penetration of $y_I=150$ mm. By comparing the above figure to that of Fig. 16a for the same simulation with value $y_I=5$ mm, we can see the change in rubble deformation patterns during the indentor penetration: The amount of downward moving rubble decreased when the y_I value increased.

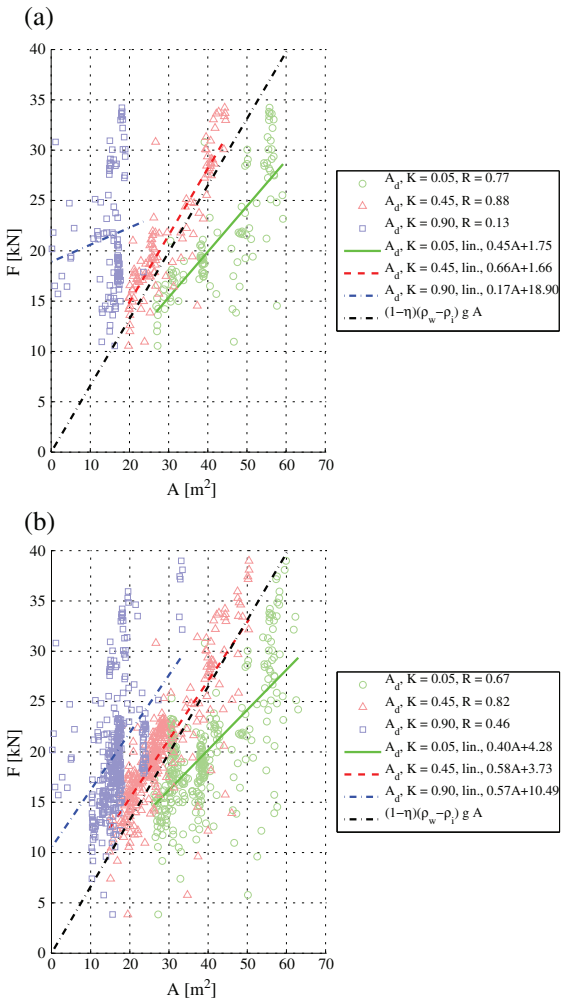

Fig. 20. The data set $F-A_d(K,y_l)$ (see text for details) when $K=\{0.1,0.5,0.9\}$ with indentor displacements of $y_l=\{20,30,40, \ldots,150\}$ mm: (a) Simulations on Ridges 1–4 with a freeze bond tensile and shear strength of $\sigma_{cr}=10$ kPa and $\tau_{cr}=50$ kPa, respectively, and (b) all simulations. The legend gives the correlation coefficients R and the linear fits of the data sets for each K. Data points from the simulations with both friction coefficients ($\mu=0.05$ and 0.3) are included in the figure.

The values of τ when using assumptions (1)-(3) for F^b are given in Table 2 for freeze bond shear strengths $\tau_{cr}=\{5,50,100\}$ kPa. The symbols $\tau^{(1)}$, $\tau^{(2)}$ and $\tau^{(3)}$ in the table refer to the *au* values derived when using assumptions (1)-(3) in previous paragraph for F^b, respectively. The data in the table is from the simulations with both friction coefficients μ, the effects of which are discussed in the next section.

As Table 2 shows, the estimate for F^b drastically affects the shear strength value derived from the experiments. With a low freeze bond shear strength τ_{cr}, $\tau^{(2)}$ and $\tau^{(3)}$ show only fairly minor difference. The reason for this is that the failure pattern with the low τ_{cr} values is close to that of the cylindrical failure: As Fig. 14 shows, with the low τ_{cr} values, the area A_p of the initial plug due to failure is fairly close to 16 m^2 of the cylindrical plug.

The difference between the $\tau^{(2)}$ and $\tau^{(3)}$ values increases with τ_{cr}, and $\tau^{(2)}$ is approximately 50% higher than $\tau^{(3)}$ with $\tau_{cr}=50$ kPa. This is due to the change in rubble failure patterns with τ_{cr}, as shown by

Table 2
Mean shear strength, τ, values with their standard deviations for different freeze bond shear strengths, τ_{cr}, and different measures for the buoyant indentor load component, F^b, in Eq. (15): The value $F^b=0$ was used for $\tau^{(1)}$, the value $F^b=11$ kN, assuming cylindrical failure, for $\tau^{(2)}$, and the value $F^b=F_b(A_p,\eta)$ from Eq. (13), while taking account the buoyant load of the plug forming in the initial failure, for $\tau^{(3)}$. In addition, the table gives the ratios of the mean shear stress values derived using the different F^b values. The table includes data from the simulations done on Ridges 1–4 with the friction coefficients $\mu=0.05$ and $\mu=0.3$ and a freeze bond tensile strength 10 kPa.

		τ_{cr} [kPa]		
		5	50	100
τ values [kPa]	$\tau^{(1)}$	3.6 ± 0.8	5.8 ± 0.9	7.0 ± 1.3
	$\tau^{(2)}$	2.3 ± 0.8	4.5 ± 0.9	5.7 ± 1.3
	$\tau^{(3)}$	2.0 ± 0.6	3.0 ± 0.6	4.2 ± 1.0
τ ratios [−]	$\bar{\tau}^{(1)}/\bar{\tau}^{(3)}$	1.79	1.96	1.68
	$\bar{\tau}^{(2)}/\bar{\tau}^{(3)}$	1.14	1.52	1.36

Fig. 14: The area A_p of the initial plug increases with τ_{cr} and is considerably higher than the area of a cylindrical plug (16 m^2). With a $\tau_{cr}>50$ kPa, the increase in τ is driven only by the increase in the rubble strength (A_p stays virtually constant with τ_{cr} for $\tau_{cr}>50$ kPa as Fig. 14 shows). As a result, τ estimates which do not properly take account the buoyant load component, improve somewhat. Still, the difference in the τ is up to 68% depending on the estimate.

4.1.2. Derivation of the material parameters

The simulations suggest that the punch through experiments may not be a suitable method for deriving the rubble internal friction angle. This observation is explained by the failure modes of the freeze bonds: The ratio of bond points failing due to tensile failure instead of shear failure under compression increased when the freeze bond shear strength, τ_{cr}, was increased. In tensile failure, friction does not affect the cohesive failure process of a bond because the bonded blocks are not in contact with one another.

In other words, the frictional resistance is not mobilized at the instant of the peak load in a punch through experiment, which has also been formerly suggested by, for example, Croasdale in Azarnejad and Brown (2001) and Liferov and Bonnemaire (2005). It should be noted here, that here the frictional resistance is due to contact friction, which is evidently related to the internal friction angle of the rubble mass, that is, a change in friction coefficient or rubble friction angle would be expected to cause similar change in the measured forces.

The failure modes of the bond points were studied here similar to Ortiz and Pandolfi (1999). For each freeze bond failure, the normal (δ_n) and tangential (δ_t) components of cohesive crack opening displacement (see Section 2) were monitored. If $\delta_n \geq |\delta_t|$ at the end of the cohesive crack growth process ($\delta_e=\delta_f$ in Fig. 4), then the failure was tensile, otherwise, the failure was due to shear. The mean ratios of the bond point tensile failures to the failures due to shear, together with the ratios of rubble shear strength, τ, with different friction coefficients μ, are collected to Table 3.

As Table 3 shows, already with a value $\tau_{cr}=5$ kPa close to half of the freeze bond failures occurred in tension (38%). Anyhow, the τ values with $\tau_{cr}=5$ kPa increase with μ, as most of the freeze bonds still fail due to shear. As the rubble gets stronger, the relative number of tensile failures increases, leading to virtually equal τ values irrespective of μ: With a value $\tau_{cr}=100$ kPa all shear strength measures $\tau^{(1)-(3)}$ indicate a virtually equal rubble shear strength with both μ, and the tensile freeze bond failures clearly dominate.

The above results suggest that in addition to the fair amount of experimental work on freeze bond shear strength under compression already conducted (Ettema and Schaefer, 1986; Repetto-Llamazares et al., 2011a,2011b; Shafrova and Høyland, 2008), the freeze bond tensile strengths should be studied in order to improve the interpretation of punch through experiment results. So far, the experimental work on freeze bond tensile strengths appears to be limited to the

Table 3
Ratios of rubble shear strength, τ, resulting from the simulations done with different friction coefficients, μ, $\tau(\mu=0.05)$, and $\tau(\mu=0.3)$, and the ratio of the number of tensile bond failures (n_t) to the number of bond failures due to shear (n_s). Shear strength measures $\tau^{(1)-(3)}$ refer to the τ values with different estimates for the buoyant load component, F^b, in Eq. (15): $F^b=0$ was used for $\tau^{(1)}$, $F^b=11$ kN, assuming cylindrical failure, for $\tau^{(2)}$, and $F^b=F_b(A_p,\eta)$ from Eq. (13) while taking account the buoyant load of the plug forming in the initial failure, for $\tau^{(3)}$. The table includes data from the simulations done on Ridges 1–4 with a freeze bond tensile strength 10 kPa.

		τ_{cr} [kPa]		
Ratio	τ measure	5	50	100
$\tau(\mu=0.3)/\tau(\mu=0.05)$ [−]	$\tau^{(1)}$	1.17 ± 0.09	1.06 ± 0.03	1.02 ± 0.01
	$\tau^{(2)}$	1.29 ± 0.12	1.07 ± 0.04	1.02 ± 0.01
	$\tau^{(3)}$	1.09 ± 0.35	1.07 ± 0.10	0.98 ± 0.12
n_t/n_s [−]		0.38 ± 0.14	1.44 ± 0.61	2.54 ± 0.91

so-called pull out tests briefly reported in Timco et al. (2000) and Croasdale et al. (2001).

4.2. Comparison to experiments and continuum models

The results from the simulations were in agreement with earlier experimental work, as shown below. Earlier modeling efforts and the results from this study are also compared below. This comparison includes two principal observations: (1) The continuum models used previously differ from the model used here, as they do not predict tensile failures within the rubble, and thus, show peak load values that are highly dependent on the rubble friction, and (2) based on the results presented here, the physical phenomena behind decreasing post-peak indentor force, which is generally accounted on the material softening in the continuum models, is related to the change in the rubble geometry.

4.2.1. Comparison to experiments

The indentor force-displacement ($F-y_I$) records in Fig. 6 show features similar to those from full-scale experiments done by Heinonen (2004): A peak load F^m occurred early in the experiments and was followed by a drop in F values. Here, the initial drop due to global plug failure was steeper than in their experiments, but Heinonen (2004) reports that in their experiments, the post-peak load decrease does not correctly present the rubble resistance due to a transient rapid motion of the indentor platen after the peak load.

The peak load, F^m, and global plug failure occurred here at a very early stage of the indentor penetration (~1 mm), as shown by Fig. 7. The indentor penetration at F^m was smaller than usually observed in the field, even if the indentor displacements at F^m have also been low in the field. In the full-scale experiments performed and analysed in Heinonen (2004), F^m occurred at an indentor displacement of $y_I=$ 8.8…18.1 mm (with a mean of 13.1 mm). Also Croasdale et al. (2001) report that the F^m and global plug failure occurred with a very small indentor penetration, but they unfortunately do not give exact indentor penetration values.

The failure patterns from the simulations can be compared to those observed in the laboratory, where detailed data on the failure patterns is available. The failure patterns are in agreement with the findings of Lemee and Brown (2002), who describe slow, small-scale punch through experiments showing a trapezoidal plug of rubble moving with the initial failure that occurred at the edges of the plug. Jensen et al. (2001) describe the failure in their experiments also having a trapezoidal plug, with the plug edges that were approximately 40° in relation to the vertical. This observation is in agreement with the failure patterns observed here, in which the angle of the plug edges was in the range of the α values in Fig. 13.

The shear strength values, τ, given in Table 2 are well within the range of those found in the literature. Croasdale et al. (2001) and Heinonen (2004) reported values $\tau=6-12.8$ kPa and $1.3-18$ kPa, respectively, both not taking account the buoyant load component ($F_b=0$ in Eq. (15), hence the results should be compared to $\tau^{(1)}$ in Table 2), and Leppäranta and Hakala (1992) $\tau=1.7…4$ kPa assuming the buoyant load component being due to cylindrical plug (comparable to $\tau^{(2)}$ in the table).

4.2.2. Comparison to earlier models

The fact that the friction coefficient had a fairly small effect on the peak load F^m was unexpected based on earlier work on punch through experiments using continuum models: In the model by Heinonen (2004) the maximum load increased with an increase in the cohesion and with an increase in the friction angle of the continuum presenting the rubble. Also, the continuum model by Serré (2011) showed a similar dependency between F^m and the friction angle for simulations without cohesion (no study on the combined effect of friction and cohesion was performed in his work).

According to Heinonen (2004), this result was due to compressive pressure increasing within the rubble due to indentor penetration. This leads to an increase in frictional resistance of the rubble on the shear planes, which then hinders rubble displacements. Furthermore, this effect becomes more prominent in his simulations with an increase in the rubble cohesion, while the model does not show tensile stresses within the pile. This tendency is very different from the observations made in ecrefphi; in those simulations tensile freeze bond failures clearly occur (see Table 3) and the simulations show vanishingly small effect of friction on F^m with high freeze bond strengths (see Fig. 10).

On the other hand, when compared to the so-called pseudo-discrete continuum model in Liferov (2005), the observations here met our expectations. Liferov (2005) reports that the effect of the friction angle on the initial failure and strength of the rubble in virtual shear box experiments was negligible. It should also be noted, that his virtual shear box experiments showed tensile freeze bond failures dominating the rubble failure process under low compressive pressures and further showed a combination of shear and tensile freeze bond failures with higher compression. These findings support the observations on the importance of the tensile freeze bond failures in Section 2.

The post-peak indentor load displacement records were similar to those in the model provided by Heinonen (2004), excluding the initial steep decrease after the maximum load, F^m, which occurred here. After this steep decrease, both models show similar behavior, as the post-peak F decreased with an increase in the indentor displacement. In Heinonen (2004), the rate $\partial F/\partial y_I$ of the decrease was affected by the internal friction of the material, with a higher internal friction causing lower rate of decrease. Increasing the friction coefficient here caused a similar change in the post-peak $\partial F/\partial y_I$, as Fig. 6 shows.

Based on the results here, our interpretation of the post-peak rubble behavior differs from that offered by the continuum models. Heinonen (2004) accounts for the decrease in the post-peak F as being due to the rubble material softening, with the details of the exact mechanism and physical phenomena being rendered out by the continuum description of the rubble. The results here clearly indicate (see Section 2 and Fig. 20 in particular) that the change in the post-peak F is due to a change in the rubble deformation patterns, that is, the post peak load is decreasing due to a change in the ridge geometry during a punch through experiment.

5. Conclusions

In this paper we introduced and described in detail a technique for modeling partly consolidated ice rubble using a two-dimensional combined finite-discrete element method. In the technique, each ice block within the rubble, the contact forces between the blocks, the block deformation, and the rubble freeze bonds are modelled. The technique for modeling freeze bonds was based on initially rigid cohesive elements.

We used the technique to the modeling of ridge keel punch through experiments on relatively thin (4 m) partly consolidated ridges. We varied the ridge keel strength by varying the shear strengths of the freeze bonds. The main findings from the simulations concerning punch through experiments with dimensions and freeze bond strengths comparable to the ones here are as follows:

- The maximum load in the experiments is dependent upon the initial failure pattern of the rubble, which, on the other hand, is dependent upon the geometry and strength of the ridge (see Sections 3.1–3.2.1).
- The post peak-load levels show a clear dependency on the rubble volume being displaced by the indentor platen during the experiment, that is, the post-peak load is a function of the buoyant load of the rubble displacing during the experiment (see Section 3.2.2).
- Incorrect assessment of the buoyant indentor load component can lead to inaccuracies when in deriving the rubble shear strength: The buoyant load component a result not only of the rubble directly under the indentor and if not correctly taken account, could lead to severe over estimation of ridge keel shear strength (see Sections 3.2.1 and 4.1.1).
- The decrease in the indentor load on the post-peak regime, usually accounted for material softening, is due to a change in the rubble mass supported by the indentor (see Figs. 18–20).
- Punch through experiments may not be a proper method for deriving the rubble friction angle for a strongly bonded ridge keel: The rubble failure process mainly involves tensile failures of the freeze bonds and the friction does not affect the peak load or the shear strength (see Section 4.1.2).

Future work should include a more detailed investigation of the reasons for the effect of the ridge geometry. This work should involve various rubble depths, block geometries and indentor widths so as to include the potential scale effects. More detailed study on the effect of the freeze bond tensile strength should also be performed to investigate whether or not the above findings apply to all freeze bond tensile to shear strength ratios. In addition, punch through experiments should be modeled in parallel to modeling of shear box experiments.

The model should also be used in parallel with continuum models, since large-scale problems are still more efficiently solved using the continuum models. On the other hand, continuum models can benefit from an understanding on the smaller scale phenomena provided by discrete models. In other words, advantage of the complementary roles of discontinuum and continuum modeling should be exploited in modeling.

Related to the experiments, work on the modeling of punch through experiments should include detailed identification of the relationships between quantities measurable during the field experiments and the material parameters. This work would make it easier to interpret the results even when only a limited number of full-scale measurements (often in very challenging environment) can be conducted.

Acknowledgments

The financial support from the Ministry of Education of Finland through the National Graduate School in Engineering Mechanics and from the Graduate Program of Aalto University, School of Engineering, is gratefully acknowledged.

References

Azarnejad, A., Brown, T., 2001. Small-scale plane strain punch tests. Journal of Cold Regions Engineering 15 (3), 135–153.
Azarnejad, A., Frederking, R., Brown, T., 1999. Ice rubble strength from small scale punch through tests. Proceedings of OMAE99, 19th International Conference on Offshore Mechanics and Arctic Engineering, pp. 1–9.
Bazant, Z.P., 2002. Scaling of sea ice fracture — Part I: vertical penetration. Journal of Applied Mechanics 69, 11–18.
Block, G., Rubin, M., Morris, J., Berryman, J.G., 2007. Simulations of dynamic crack propagation in brittle materials using nodal cohesive forces and continuum damage mechanics in the distinct element code LDEC. International Journal of Fracture 144 (3), 131–147.
Bruneau, S., Crocker, G., McKenna, R., Croasdale, K., Metge, M., Ritch, R., Weaver, J., 1998. Development of techniques for measuring in situ ice rubble shear strength. Ice in Surface Waters. Proc. of the 14th International Symposium on Ice, vol. 2. IAHR, pp. 1001–1007.
Camacho, G., Ortiz, M., 1996. Computational modeling of impact damage in brittle materials. International Journal of Solids and Structures 33 (20–22), 2899–2938.
Croasdale, K.R., Bruneau, S., Christian, D., Crocker, G., English, J., Metge, M., Ritch, R., 2001. In-situ measurements of the strength of first-year ice ridge keels. Proceedings of the 16th International Conference on Port and Ocean Engineering under Arctic Conditions, POAC'01, vol. 3, pp. 1445–1454. Ottawa, Ontario, Canada.
Cundall, P., Strack, O., 1979. A discrete numerical model for granular assemblies. Géotechnique 29, 47–65.
Dempsey, J., Adamson, R., Mulmule, S., 1999. Scale effects on the in-situ tensile strength and fracture of ice. Part II: first-year sea ice at resolute, N.W.T. International Journal of Fracture 95 (1), 347–366.
Dempsey, J., Tan, L., Wang, S., 2010. An isolated cohesive crack in tension. Continuum Mechanics and Thermodynamics 22 (6), 617–634.
Ettema, R., Schaefer, J.A., 1986. Experiments on freeze-bonding between ice blocks in floating ice rubble. Journal of Glaciology 32 (112), 397–403.
Frederking, R., Barker, A., 2002. Friction of sea ice on various construction materials. Proceedings of the 16th IAHR International Symposium on Ice, vol. 1, pp. 442–449.
Geuzaine, C., Remacle, J., 2009. Gmsh: a three-dimensional finite element mesh generator with built-in pre- and post-processing facilities. International Journal for Numerical Methods in Engineering 79 (11), 1309–1331.
Gürtner, A., 2009. Experimental and Numerical Investigations of Ice-Structure Interaction. Doctoral Theses, NTNU, Trondheim, Norway, 2009, 182 p, ISBN 978-82-471-1420-9.
Haase, A., Polojärvi, A., Tuhkuri, J., 2010. 3D discrete numerical modeling of conical structure-ice rubble interaction. Proceedings of 20th IAHR International Symposium on Ice. IAHR, Lahti, Finland (electronic publication).
Heinonen, J., 2004. Constitutive modeling of ice rubble in first-year ridge keel. Doctoral Thesis, TKK, VTT Publications 536. Espoo, Finland, 2004, 142 p, ISSN 1235–0621.
Heinonen, J., Määttänen, M., 2000. Ridge loading experiments, field experiments in winter 2000. LOLEIF Progress Report No. 10. TKK . 40 pp.
Heinonen, J., Määttänen, M., August 12–17 2011a. Full-scale testing of ridge keel mechanical properties in loleif project. Proceedings of the 16th International Conference on Port and Ocean Engineering under Arctic Conditions, POAC'01, vol. 3. Canadian Hydraulics Centre, Ottawa, Ontario, Canada, pp. 1435–1444.
Heinonen, J., Määttänen, M., 2001b. Ridge keel mechanical properties — testing. Field experiments in winter 2001. ReportSTRICE. TKK . 39 pp.
Hopkins, M., 1992. Numerical simulation of systems of multitudinous polygonal blocks. Tech. Rep. 92–22. Cold Regions Research and Engineering Laboratory, CRREL. 69 pp.
Hopkins, M., 1998. Four stages of pressure ridging. Journal of Geophysical Research 103 (C10), 21,883–21,891.
Hopkins, M., Tuhkuri, J., Lensu, M., 1999. Rafting and ridging of thin ice sheets. Journal of Geophysical Research 104 (C6), 13605–13613.
Høyland, K.V., Løset, S., 1999. Measurements of temperature distribution, consolidation and morphology of a first-year sea ice ridge. Cold Regions Science and Technology 29 (1), 59–74.
Jensen, A., Løset, S., Høyland, K.V., Liferov, P., Heinonen, J., Evers, K.-U., Määttänen, M., 2001. Physical modeling of first-year ice ridges — part II: mechanical properties. Proceedings of the 16th International Conference on Port and Ocean Engineering under Arctic Conditions, POAC'01, vol. 3. Canadian Hydraulics Centre, Ottawa, Ontario, Canada, pp. 1493–1502.
Kuroiwa, D., 1961. A study of ice sintering. Tellus 13 (2), 252–259.
Lemee, E., Brown, T., 2002. Small-scale plane strain punch tests. Ice in the Environment: Proceedings of the 16th IAHR International Symposium on Ice, Dunedin, New Zealand, vol. 2, pp. 1–7.
Leppäranta, M., Hakala, R., 1989. Field measurements of the structure and strength of first-year ice ridges in the baltic sea. Eighth International Conference on Offshore Mechanics and Arctic Engineering, Hague, Netherlands, vol. 4, pp. 169–174.
Leppäranta, M., Hakala, R., 1992. The structure and strength of first-year ice ridges in the Baltic Sea. Cold Regions Science and Technology 20 (3), 295–311.
Liferov, P., 2005. Ice rubble behavior and strength: Part II. modeling. Cold Regions Science and Technology 41 (2), 153–163.
Liferov, P., Bonnemaire, B., 2005. Ice rubble behavior and strength: Part I. review of testing and interpretation of results. Cold Regions Science and Technology 41, 135–151.
Liferov, P., Jensen, A., Høyland, K., 2003. 3D finite element analysis of laboratory punch tests on ice rubble. Proceedings of the 17th International Conference on Port and Ocean Engineering under Arctic Conditions, POAC'03, vol. 2. Department of Civil and Transport Engineering, Faculty of Engineering Science and Technology, Norwegian University of Science and Technology, NTNU, Trondheim, Norway, pp. 611–621.
Lishman, B., Sammonds, P., Feltham, D., Wilchinsky, A., 2009. The rate- and state-dependence of sea ice friction. Proceedings of the 20th International Conference on Port and Ocean Engineering under Arctic Conditions, POAC 09 (electronic publication).
Morris, J.P., Rubin, M., Block, G., Bonner, M., 2006. Simulations of fracture and fragmentation of geologic materials using combined FEM/DEM analysis. International Journal of Impact Engineering 33 (1–12), 463–473.
Mulmule, S., Dempsey, J., 1997a. A viscoelastic fictitious crack model for the fracture of sea ice. Mechanics of Time-Dependent Materials 1 (4), 331–356.

Mulmule, S., Dempsey, J., 1997b. Stress-separation curves for saline ice using fictitious crack model. Journal of Engineering Mechanics 123 (8), 870–877.
Mulmule, S., Dempsey, J., 1999. Scale effects on sea ice fracture. Mechanics of Cohesive-Frictional Materials 4 (6), 505–524.
Munjiza, A., 2004. The combined finite-discrete element method. John Wiley & Sons Ltd., Chichester, England.
Munjiza, A., Andrews, K., 2000. Penalty function method for combined finite-discrete element systems comprising large number of separate bodies. International Journal for Numerical Methods in Engineering 49 (11), 1377–1396.
Munjiza, A., Owen, D., Bićanić, N., 1995. A combined finite-discrete element method in transient dynamics of fracturing solids. Engineering Computations 12, 145–174.
Ortiz, M., Pandolfi, A., 1999. Finite-deformation irreversible cohesive elements for three-dimensional crack propagation analysis. International Journal for Numerical Methods in Engineering 44, 44–1267.
Paavilainen, J., Tuhkuri, J., 2012. Parameter effects on simulated ice rubbling forces on a wide sloping structure. Cold Regions Science and Technology 81, 1–10.
Paavilainen, J., Tuhkuri, J., Polojärvi, A., 2006. Discrete element simulation of ice pile-up against an inclined structure. Proceedings of the 18th International Symposium on Ice, vol. 2. IAHR, pp. 177–184.
Paavilainen, J., Tuhkuri, J., Polojärvi, A., 2009. 2D combined finite–discrete element method to model multi-fracture of beam structures. Engineering Computations 26 (6), 578–598.
Paavilainen, J., Tuhkuri, J., Polojärvi, A., 2011. 2D numerical simulations of ice rubble formation process against an inclined structure. Cold Regions Science and Technology 68 (1–2), 20–34.
Papoulia, K.D., Vavasis, S.A., 2003. Time continuity in cohesive finite element modeling. International Journal for Numerical Methods in Engineering 58, 701.
Polojärvi, A., Tuhkuri, J., 2009. 3D discrete numerical modeling of ridge keel punch through tests. Cold Regions Science and Technology 56 (1), 18–29.
Polojärvi, A., Tuhkuri, J., 2012. Velocity effects in laboratory scale punch through experiments. Cold Regions Science and Technology 70, 81–93.
Polojärvi, A., Tuhkuri, J., Korkalo, O., 2012. Comparison and analysis of experimental and virtual laboratory scale punch through tests. Cold Regions Science and Technology 81, 11–25.
Pritchard, R.S., Knoke, G.S., Echert, D.C., 2011. Sliding friction of sea ice blocks. Cold Regions Science and Technology 76–77, 8–16.
Repetto-Llamazares, A., Høyland, K., Ekaterina, K., 2011a. Experimental studies on shear failure of freeze-bonds in saline ice: Part II: ice–ice friction after failure and failure energy. Cold Regions Science and Technology 65 (3), 298–307.
Repetto-Llamazares, A., Høyland, K., Evers, K.-U., 2011b. Experimental studies on shear failure of freeze-bonds in saline ice: Part I: Set-up, failure mode and freeze-bond strength. Cold Regions Science and Technology 65 (3), 286–297.
Sam, C.-H., Papoulia, K.D., Vavasisc, S.A., 2005. Obtaining initially rigid cohesive finite element models that are temporally convergent. Engineering Fracture Mechanics 72 (14), 2247–2267.
Sayed, M., Timco, G.W., Sun, L., 1992. Testing model ice rubble under proportional strains. OMAE 1992, Proceedings of the 11th International Conference On Offshore Mechanics and Arctic Engineering, vol. IV. Arctic/Polar Technology.
Schreyer, H.L., Sulsky, D.L., Munday, L.B., Koon, M.D., Kwok, R., 2006. Elastic-decohesive constitutive model for sea ice. Journal of Geophysical Research 111 (C11S26).
Serré, N., 2011. Mechanical properties of model ice ridge keels. Cold Regions Science and Technology 67 (3), 89–106.
Shafrova, S., Høyland, K., 2008. The freeze-bond strength in first-year ice ridges. small-scale field and laboratory experiments. Cold Regions Science and Technology 54 (1), 54–71.
Timco, G., Weeks, W., 2010. A review of the engineering properties of sea ice. Cold Regions Science and Technology 60 (2), 107–129.
Timco, G., Croasdale, K.R., Wright, B., 2000. An overview of first-year sea ice ridges. Tech. Rep. 5–112. PERD/CHC.
Tuhkuri, J., Polojärvi, A., 2005. Effect of particle shape in 2D ridge keel deformation simulations. Proceedings of the 18th International Conference on Port and Ocean Engineering under Arctic Conditions, POAC'05, vol. 2. Clarkson University, Potsdam, New York, USA, pp. 939–948.